INFLUENCE OF SENSOR LOCATION IN REMOTE-SENSOR BASED FLOW ESTIMATION

Anna Amani

Department of Mechanical & Manufacturing Eng.
University of Calgary
2500 University Dr. NW, Calgary, Alberta, Canada
aamani@ucalgary.ca

Robert J. Martinuzzi

Department of Mechanical & Manufacturing Eng.
University of Calgary
2500 University Dr. NW, Calgary, Alberta, Canada
rmartinu@ucalgary.ca

ABSTRACT

A strategy is developed for improving sensor-based flow field estimations for remotely-placed sensors *i.e.,* not contiguous to the estimated field. The remote sensors are arrays of surface-pressure measurements. The velocity field is obtained from planar stereoscopic PIV. The pressure field is first augmented using a classical multi-time delay technique. Subject to a proper orthogonal decomposition, both fields are recast in an optimal subspace. It is shown that additional improvements in the estimation, quantified by a reduction of the estimation residual and increase in the resolved coherent contributions to the Reynolds stress fields, are achieved by incorporating optimized mode-specific delays between PIV and sensor subspaces. The methodology and results are illustrated in the estimation of the quasi-periodic turbulent flow in the wake of a surface mounted square-base pyramid.

INTRODUCTION

Flow estimation based on sensor data physically located outside the direct domain of interest is an important technique for applications such as flow monitoring or feedback control and a diagnostic tool for volumetric reconstructions of the coherent contributions to fluctuating velocity fields from uncorrelated data (Hosseini et al., 2015). However, synchronizing the dynamics between the flow field and remote-sensor data for different scales of motion remains an important challenge estimation quality.

As previously shown, the inclusion of global time delays in linear stochastic estimation (LSE) can improve the rendering of the flow dynamics (Hudy & Naguib, 2007). Durgesh & Naughton (2010) show that further improvements are obtained for periodic flows by implementing a multi-time delay technique. These studies lead to the observation that estimation optimization requires accounting for different scales of motion. While spectral techniques (*cf.* Tinney it et al., 2008) successfully exploit this observation, the application of spectral-techniques to real-time estimation is severally limited. Hosseini *et al.* (2015), however,

show that expanding the velocity file in an optimal orthogonal space allows synchronizing velocity and sensor data for different scales of motion for time-domain estimation.

In this work, the technique of Hosseini *et al.* (2015) is extended to remote-sensing applications. For diagnostic purposes, the method is illustrated for the case of the quasi-periodic wake of a surface-mounted square-based pyramid protruding a thin boundary layer. This flow is characterized by the strongly modulated periodic and base flow modulations, thus allowing to consider different scales of motion.

METHODOLOGY

Experimental Setup

The measurements were conducted in a suction type open-test-section wind tunnel. The geometry and nomenclature are summarized in Fig. 1. A square based pyramid with height and base width of $h = 39$ mm and $d = 45$ mm, and apex angle $\zeta = 60°$ was mounted on a sharp-leading-edge flat plate. The thickness of the boundary layer at the location of the pyramid with the pyramid remover was $\delta/h = 0.25$. The free stream velocity was $U_\infty = 10 m/s$, corresponding to a Reynolds number $Re_d = U_\infty d/\nu = 28000$, with turbulence intensity of 0.8%.

A LaVision Flow Master stereoscopic PIV system was used to measure the velocity vectors (u, v, w) at horizontal $(x - y)$ planes. Image pairs with a time with a time separation of $18 \mu s$ were taken at a rate of $f_s = 500 Hz$ capturing 10 data points per shedding cycle. Interrogation windows of 32×32 pixels with 50% overlap (giving a vector spacing of 1.2 mm) were used to calculate the velocity vectors. For each plane 6000 image pairs were obtained spanning 600 shedding cycles. The fluctuating pressure at the pyramid side faces ($z/d = 0.22, 0.45, 0.68$ at either sides) and the flat plate ($x/d = 1.5, 2$ at $y/d = \pm 0.25$) were taken simultaneously with the velocity data at a sample rate of $10.24 kHz$.
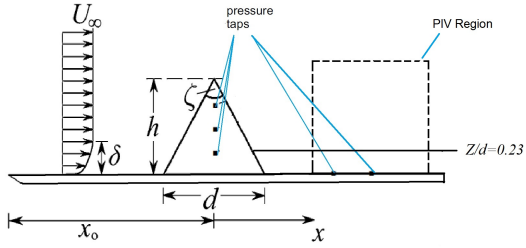
1

Figure 1: Schematic of the experimental set-up, nomenclature and the position of the pressure taps. Box with broken line indicates the range of PIV observations windows. Solid line indicates the plane z/d=0.23.

Figure 2: Instantaneous sectional streamlines superposed with iso-contours of the Ω_z-vorticity of measured velocity field at the plane z/d=0.23 for an arbitrary PIV-snapshot.

FLOW ESTIMATION

Staring with the procedure of Hosseini *et al.* (2015), the velocity field is expanded onto the orthonormal basis $\mathbf{u}(\mathbf{x},t) = \sum_{k=1}^{N} a_u^{(k)}(t)\phi(\mathbf{x})$ where $\phi_u^{(k)}$ are the empirical basis vectors and $a_u^{(k)}$ the temporal modal coefficients from a proper orthogonal decomposition (POD). The pressure data (the remote-sensors) are augmented using time-delayed virtual sensors as per the multi-time delay technique. The augmented pressure field is then expanded onto an orthonormal basis using POD.

Following this procedure, the correlation of the pressure coefficients and the spatio-temporal velocity data $< a_p^{(n)}, \mathbf{u}(\mathbf{x},t) >$ reduce to correlations between temporal coefficients. This great simplification makes it now possible to extract mode-specific correlations.

The technique is now extend to optimize the estimation by considering the mode-specific time delays, τ_n, such that the estimated velocity modal coefficients are

$$\hat{a}_u^{(k)}(t_{est}) = \sum_n = 1^{N_p} a_p^{(n)}(t_{est} - \tau_n) < a_p^{(n)}(t - \tau_n), a_u^{(k)}(t) > /\lambda_p^{(n)}$$

where τ_n are determined by maximizing the pressure-velocity correlation coefficients. The estimated flow filed is then obtained as: $\hat{\mathbf{u}}(\mathbf{x},t) = \sum_{k=1}^{N} \hat{a}_u^{(k)}(t_{est})\phi_u^{(k)}(\mathbf{x})$.

RESULT

To characterize the influence of the remote-sensor location on the flow field estimation, the ten wall pressure sensors shown in Fig. 1 are separated in two groups. In the subsequent figures and discussion, the estimations of the wake flow field using: the six sensors on the pyramid side faces are designated as "6F-sensors"; using the four sensors in the pyramid wake are designated "4W-sensors" and estimations based using all ten sensors are identified by "10-sensors". In Fig. 2 the raw (u, v) sectional streamlines for a single reference PIV snapshot are shown for the plane $z/d = 0.23$. Flooded iso-contours of the instantaneous vorticity field are superposed The main topological feature are the focus at $(x/d, y/d) \approx (1.5, -0.35)$, denoting the core of a recently shed vortex (counter-clockwise rotation) and the downstream extremity of a newly forming vortex penetrating the field of view in the region $x/d = 0.8$, $-0.2 < y/d < 0.3$.. Note the deflected shear layer between these foci, highlighted by the concentration of streamlines
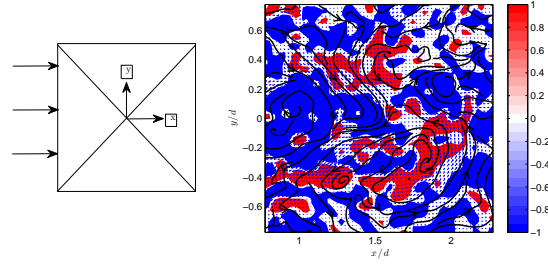
crossing the obstacle base region. Downstream features are associated with high-frequency turbulent fluctuations and do not represent a significant energetic contribution in the POD-sense.

Figure 3(*a*) shows a POD-reconstruction of the flow field in terms of sectional streamlines and *z*-component of vorticity as flooded iso-contours, in the plane $z/d = 0.23$ at the time instant corresponding to that shown in Fig. 2. The reconstruction consist of the five most energetic POD modes, which account approximately for 70% of the total fluctuation energy: A slow-drift modes, representing approximately 6% of the total fluctuation energy and for which most of the spectral energy contributions occur at frequencies significantly lower than the shedding frequency; the 1st-harmonic pair for which a significant spectral peak is observed at the shedding frequency representing approximately 56% of the total fluctuation energy; and 2nd-harmonic pair contributing about 8% of the total fluctuation energy. The two main topological features corresponding to the forming and shed vortices can be distinctly identified. The coherent contribution to the vorticity field now clearly shows high-concentration levels in the large-scale vortices.

The estimated flow field for this plane using the six side face 6F-sensors and four plate 4W-sensors as estimators are shown in Fig. 3(*b*) and (*c*), respectively. For these estimations, a traditional multi-time delay is implemented directly following a classical methodology, without accounting for mode specific signal lag between the sensor and PIV fields. The 6F-sensor estimation provides a poor estimation of the velocity field. Considering the shed vortex, the location of its core is significantly displaced towards the $y > 0$ side of the obstacle. The coherent contribution to the vorticity field is severely underestimated and the high-vorticity regions are discontinuous. The forming vortex is also displaced upstream of the observation domain. The 4W-sensor estimation are closer to the original field, but a misalignment of the vortex structure is still observed. This misalignment suggests that a phase-lag between the velocity and pressure (sensor) fields still exists. This observation is perhaps surprising, since the four wall sensors are located directly below the PIV plane. However, it is noted that a lag may also arise from the response characteristics of the tapping-line-sensor system. More significantly, however, is that the vorticity field magnitude appears underestimated in the core region of the vortex and overestimated towards the downstream end of the observation domain.

The estimations conducted to account for the mode-specific lag between the sensors and PIV fields are consid-
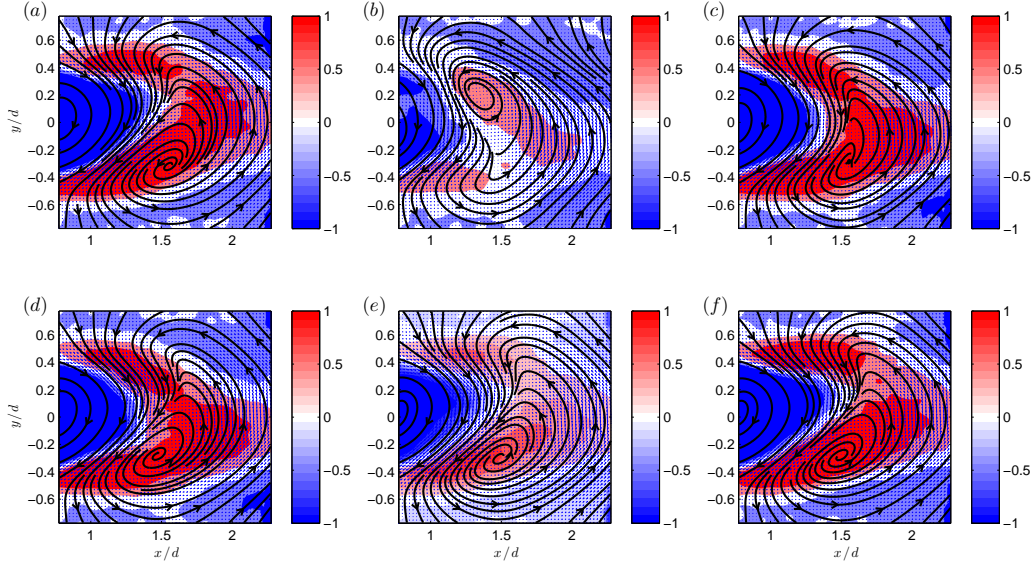
2

Figure 3: Sectional streamlines of the coherent contribution to the instantaneous velocity superposed with Ω_z-vorticity in the plane z/d=0.23 for the same time instant as in Fig. 2: (a) coherent reconstructed velocity field with five most energetic POD-modes; (b) estimated with 6F-sensor arrangement without time lag (c) estimated with 4W-sensor arrangement without time lag. Estimations with optimised time lag: d) 10-sensor; (e) 6F-sensor; and (f) 4W-sensor arrangements.

ered next. The optimised estimations for the same time instant and plane shown in Fig. 2 are presented for the three different sensor arrangements in Fig. 3(d)-(f) to facilitate comparison. As expected, the values of the mode-specific lags obtained for the three sensor arrangements differ. However, for a given sensor arrangement, it is found that it is sufficient to estimate τ_Δ for the slow-drift mode and only one value, τ_h, for the harmonic pairs. By construction, the mode-specific lag must be identical for the two modes of a given harmonic pair. However, the lag values calculated for the first and second harmonic pairs differed by less than 0.5% and thus τ_h was assumed to be the same for all four harmonic modes.

From Fig. 3(d), it is seen that the 10-sensor estimation is nearly optimal and matches very well with the original direct POD-reconstruction given in Fig. 3(a). The topology of the instantaneous streamlines cannot be easily differentiated and the location of the vortex centers match well. The vorticity distribution is also closely matched.

The optimised reconstruction using the four sensors on the wall in the wake, denoted 4W-sensor, is shown in Fig. 3(f). When compared to the non-optimised reconstruction in Fig. 3(c), changes in the streamline topology are observed. The optimisation results in better defined foci in the vortex cores. The location of the foci now closely matches that observed in Fig. 3(a). The estimation of the vorticity field is greatly improved. The distribution more closely resembles the original POD-reconstruction and the regions of overestimation have been eliminated. It remains, however, that the curvature of the upper shear layer is less well estimated when compared to the 10-sensor case.

The most dramatic effect is observed for the 6F-sensor case, where the six sensors are located on the obstacle side faces and upstream of the PIV observation domain. In the optimised estimation, Fig 3(e), the topology of the streamlines is much closer to that observed from the direct POD-

reconstruction and predicted locations of the foci is significantly improved. The magnitude of the vorticity field is still somewhat underestimated, but the distribution now resembles that of the original field. In particular, the shear layer is now resolved and the connectivity of the different regions is significantly improved.

In Fig. 4, the different estimation using 10-sensors, 6F-sensors (with and without lag) are compared to the measured time evolution for a firstharmonic and slow-drift, a_Δ, modal coefficient. Figure 5 shows the corresponding residuals. As expected, using all 10 sensors generally provides a better estimation than using 6F-sensors. The inclusion of τ_h improves mainly the synchronisation of the shedding phase. The estimated amplitude of the harmonic coefficient is improved to a much less extent. Including τ_Δ has little influence on the estimation of the amplitude of a_Δ. When considering the residuals of the 6F-sensor, the residuals are only marginally improved.

Despite the minor improvement in the residuals for the estimation a_Δ with the 6F-sensor arrangement, the addition of τ_Δ and τ_h greatly improve the estimation using the 6F-sensor arrangement as seen when comparing Fig. 3(f) and 3(a). Moreover, not including τ_Δ results in a poor estimation using the 6F-sensor arrangement, as was observed earlier by Hosseini et al. (2015). This observation highlights the importance of estimating not only the amplitude, but also the correct synchronisation between the modes. The synchronisation yields the trajectory of the flow solution in the modal space. Hence, albeit subtle, inclusion of τ_Δ and τ_h modifies the solution trajectory and thus the quality of the estimation.

It should be noted that τ_Δ and τ_h are quite different in terms magnitude and not linearly related. For example, when comparing the lag values obtained for the 4W-senor and 6F-sensor estimations, τ_h was greater for the 6F-sensor than for 4W-sensor case, while τ_Δ was less. These results
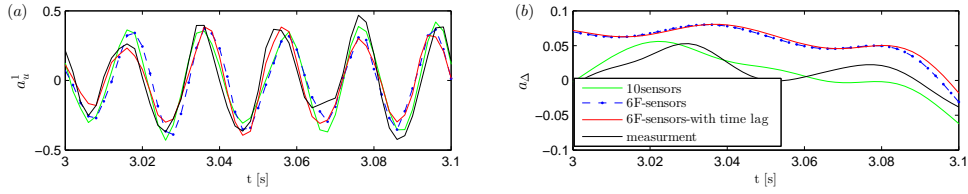
3

Figure 4: Estimation of the temporal coefficient with and without time lag implementation at the plane z/d=0.23 for 10-sensor and 6F-sensor arrangements: (*a*) first harmonic coefficient a^1 (*b*) slow-drift coefficient a_Δ.
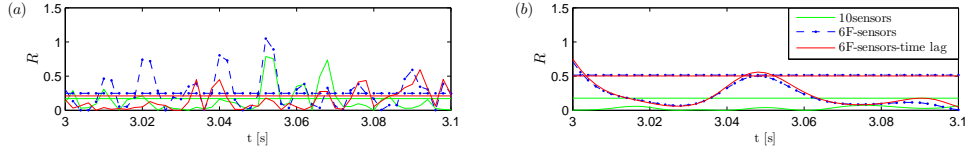

Figure 5: Residual of the temporal coefficient with and without time lag implementation at the plane z/d=0.23 for 10-sensor and 6F-sensor arrangements: (*a*) first harmonic coefficient a^1 (*b*) slow-drift coefficient a_Δ.

thus indicate that accounting for the specific mode lag is a more effective means of improving estimations from remote sensors than using a single "global" lag as is commonly done in implementing the LSE-technique.

The relative contribution of coherent and incoherent fluctuations to the Reynolds stress field is of fundamental interest. The velocity field is subject to the triple decomposition:

$$u_i(\mathbf{x},t) = U_i(\mathbf{x}) + u_{ci}(\mathbf{x},t) + u_i''(\mathbf{x},t),$$

where the subscript "*i*" denotes the Cartesian component, U_i is the long-term mean, u_{ci} the coherent contribution obtained from the estimation of the five most energetic POD-modes and u_i'' is the incoherent (residual) contribution. The arguments $\mathbf{x}$ and t denote the position vector and time, respectively. For compactness, these arguments are implied in the following discussion. By construction, the coherent and incoherent fields are uncorrelated such that the total stresses are simply:

$$\overline{u_i'u_j'} = \overline{u_{ci}u_{cj}} + \overline{u_i''u_j''}.$$

Figure 6 presents the total Reynolds stresses $\overline{u'^2}$, $\overline{v'^2}$ and $\overline{u'v'}$ as obtained from the PIV measurements and the coherent contributions to these Reynolds stresses, $\overline{u_c^2}$, $\overline{v_c^2}$ and $\overline{u_c v_c}$ as obtained from the optimised estimations for the three different sensor arrangements.

The estimations using the 10-sensor arrangement has the lowest overall residual and captures approximately 60% of the total fluctuation energy, which compares well with the direct 5-mode POD-reconstruction which accounts for roughly 70% of the total fluctuation energy. However, the coherent contribution is not uniformly distributed over the Reynolds stresses. The v'-fluctuations, owing to the vortex shedding process, contain a much larger coherent contribution such that the $\overline{v'^2}$ and $\overline{v_c^2}$ fields are similar in spatial distribution and overall magnitude – Fig. 6(*b*) and (*e*). The $\overline{u_c^2}$ contirbution ot the overall Reynolds stress is lower, Fig. 6(*a*) and (*d*. As may be expected, maxima in $\overline{u_c^2}$ occur closer to the end of the formation region when compared to $\overline{u'^2}$. The Reynolds shear stresses are expected to result

from anisotropy, which in the near wake is closely related to the strain field resulting from the large-scale motions and deformations due to the vortex shedding process. It is thus not surprising that the $\overline{u'v'}$ and $\overline{u_c v_c}$ fields are very similar quantitatively. Hence, the estimations using the 10-sensor arrangement are a reasonable guide for assessing the effectiveness of the optimisation process when considering sensors placed at different locations.

In general, the distribution of the Reynolds stresses obtained from the optimized estimations are qualitatively very similar. The coherent contribution to the normal stresses estimated from the wall sensors placed in the wake (4W-sensor) are very similar to the 10-sensor estimations quantitatively as well. However, the estimated magnitude of $\overline{u_c v_c}$ is somewhat lower. The 4W-sensor estimations capture approximately 55% of the total fluctuation energy. The difference is mainly associate with an underestimation of the slow-drift coefficient a_Δ. While the energetic contribution of this mode is small compared to the first harmonic pair, the slow-drift variation plays an important role in describing the flow anisotropy.

In considering the estimations obtained using the six sensors on the obstacle face (6F-sensor), it is first noted that the non-optimised estimations of the Reynolds stresses differ significantly from those shown in Fig. 6. These differences are expected based on the deficiencies already observed in comparing the velocity estimations shown in Fig. 3(*b*) and *e*) and are thus not shown for brevity. Once optimised, however, the 6F-sensor estimations are qualitatively similar to those previously described. The optimised 6F-sensor estimations capture approximately 45% of the total fluctuation energy. Hence, it is not surprising that the normal stresses are underestimated – Fig. 6(*j*),(*k*). In contrast, the estimated magnitude of $\overline{u_c v_c}$ in Fig. 6(*l*) more closely matches that from the 10-sensor arrangement of Fig. 6(*f*). Is is noted that the slow-drift component is more strongly expressed when using the sensors mounted on the face of the obstacle.

Once optimised, the remote 6F-sensors also provide a fair estimation of the Reynolds stress field, albeit the magnitude is underestimated. The results show that accounting for mode-specific lag does improve the quality of the estimation, but it also highlights that the influence of the POD-modes is expressed differently on sensors located at different locations.
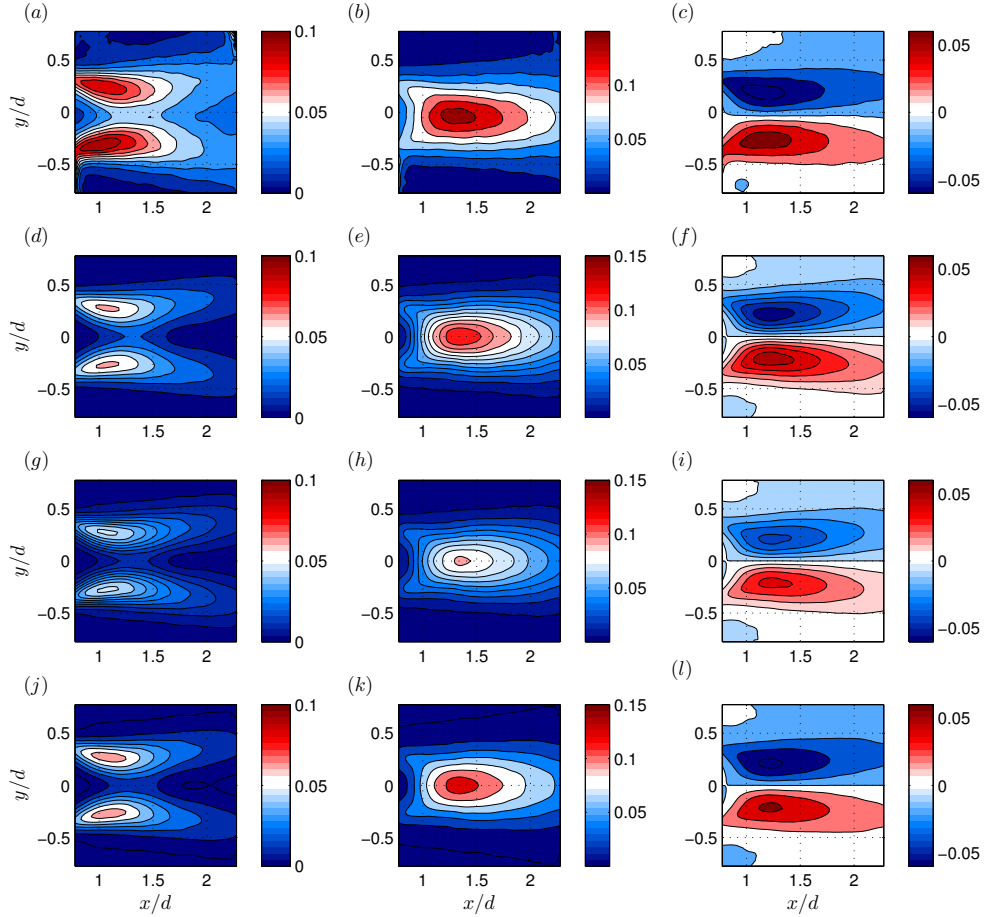
4

Figure 6: Reynolds stresses in the plane $z/h = 0.23$. Total stresses as measured directly from PIV (a) $\overline{u'^2}$, (b) $\overline{v'^2}$ and (c) $\overline{u'v'}$. Coherent contribution to the Reynolds stresses for 10-sensor arrangement: (d) $\overline{u_c^2}$; (e) $\overline{v_c^2}$; (f) $\overline{u_c v_c}$; for 6F-sensor arrangement: (g) $\overline{u_c^2}$; (h) $\overline{v_c^2}$; (i) $\overline{u_c v_c}$; for 4W-sensor arrangement: (j) $\overline{u_c^2}$; (k) $\overline{v_c^2}$; (l) $\overline{u_c v_c}$.

A fundamentally interesting application of the estimation technique is the volumetric reconstruction of the coherent fluctuating velocity field from uncorrelated PIV planar measurements. An example at two arbitrarily chosen shedding phases is shown in Fig. 7, comparing the estimated global fields obtained using the optimized 10-sensor and 6F-sensor estimations. The shedding cycles are selected for $a_\Delta \approx 0$, corresponding approximately to the average shedding cycle (*i.e.* close to the limit cycle). The PIV measurements consists of 17 xy-planar fields measured at equidistant intervals over the PIV observation domain schematically shown in Fig. 2. Pressure measurements are obtained simultaneously for each plane. The POD analysis is conducted and optimal values of τ_Δ and τ_h are obtained for each field. The estimation is then conducted for a common sensor time series.

Figure 7 shows the iso-surface of the vortex-core identification $\lambda_2 \approx -0.01$. The coherent contribution to the Ω_x component of the vorticity vector is shown in the plane $x/d = 1.5$ as iso-contours. Solid lines indicate positive and broken lines indicate negative values. The two reconstructions show very similar vortex-core features extending from the base recirculation region. These vortex skeletons represent the highly distorted and streamwise elongate shed vor-

tices. The Ω_x iso-contours match well with the location of these cores and further allow to identify interaction regions with the boundary layer and extensions of the horseshoe vortex, seen at the edges of the near the wall (ground plane) of the observation domain. This sequence of images shows similar evolution of structures and coherent-vorticity distribution, suggesting that both reconstructions render similar underlying vortex dynamics. However, these also indicate that the intensity of the vorticity field is rendered with somewhat lower fidelity using the 6F-sensor arrangement than with the 10-sensor arrangement (recalling that the 10-sensor estimations were very close to the direct POD reconstruction in each plane). This sample reconstruction highlights that an effect synchronisation has been achieved and a reasonable rendition of the flow structure can be obtained.

Once optimized, the remote 6F-sensors provide a fair estimation of the Reynolds stress field, albeit the magnitude is underestimated, and the underlying flow dynamics is rendered. The results show that accounting for mode-specific lag is an effective strategy for increasing the reliability of the estimation even for sensors significantly removed from the observed flow field.
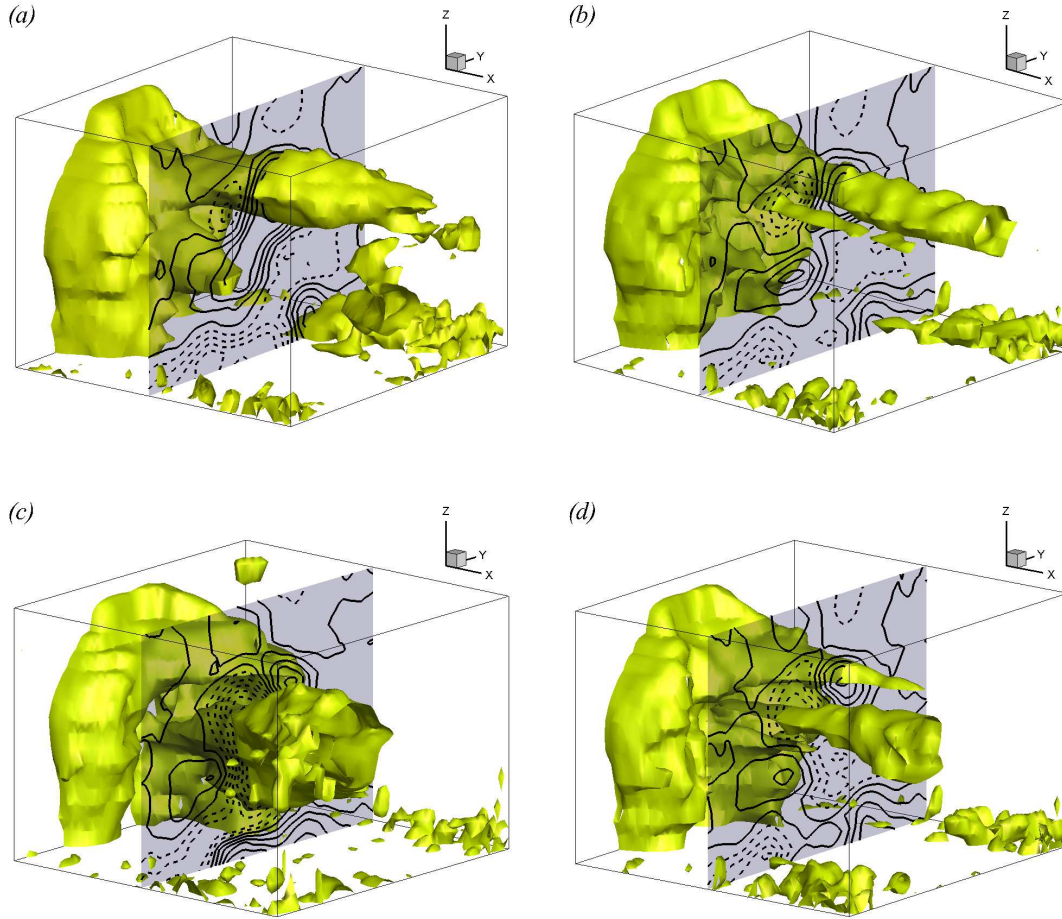
5

Figure 7: Isometric view of the volumetric reconstruction of the coherent fluctuating flow field. Iso-surfaces of $\lambda_2 = -0.01$ and iso-contours of Ω_x vorticity component in the plane $x/d = 1.5$ are shown at two arbitrarily chosen shedding phases at $a_\Delta \approx 0$, corresponding approximately to the average shedding cycle: (*a*), (*c*) reconstruction using optimised 10-sensor estimator; (*b*), (*d*) using 6F-sensor estimator.

CONCLUSION

A strategy and methodology for improving estimations of the coherent contributions to the velocity field fluctuations from remote sensors (*i.e.* sensors at locations not contiguous with the flow field observation domain) has been illustrated. Subject to a modal decomposition of both the velocity and estimator (sensor) fields, it is shown that considering optimising the mode-specific time lag can significantly increase the estimation quality and the ability to adequately render important aspects of the flow dynamics.

Closer inspection of the results from differently located sensor arrangements allows for important observations:

- Implementation of the optimised mode-specific time-lags generally reduces the residuals. However, a net reduction of the residuals is not a sufficient condition for improving the estimation of flow dynamics.
- The proper synchronisation of the different modes in the estimated field is critical to rendering the correct dynamics in the flow and as a consequence the coherent contribution to the Reynolds stress field. This observation suggests that the prediction of the solution trajectory in the modal phase-space is an important el-

ement in estimating the dynamics.
- The strength of different modes is not expressed uniformly in the flow field such that the effectiveness of the optimisation remains location dependent.

REFERENCES

Durgesh, V. & Naughton, J.W., 2010, "Mult-time-delay LSE-POD complementary approach applied to unsteady high-Reynolds-number near wake flow," *Exp. Fluids* (**49**), 571-583.

Hosseini, Z., Martinuzzi, R. J. & Noack, B.R., 2015, "Sensor based estimation of the velocity in the wake of a low-aspect-ratio pyramid," *Exp. Fluids* (**56**), 13.

Hudy, L., & Naguib, A., 2007, "Stochastic estimation of separated-flow field using wall-pressure-array measurements," *Phys. Fluids* (**19**) 024103.

Tinney, C.E., Ukeiley, L.S., & Glauser, M.N., 2008, "Low-dimensional characteristics of a transonic jet. Part 2. Estimate and far-field prediction," *J. Fluid Mech.* (**615**), 53-92.

6